Hindawi
Computational Intelligence and Neuroscience
Volume 2022, Article ID 5371350, 14 pages
https://doi.org/10.1155/2022/5371350

Research Article

A Lightweight Dangerous Liquid Detection Method Based on Depthwise Separable Convolution for X-Ray Security Inspection

Dongming Liu,[1,2] **Jianchang Liu**,[1,2] **Peixin Yuan**,[3] **and Feng Yu**[1,2]

[1]*College of Information Science and Engineering, Northeastern University, Shenyang 110819, China*
[2]*State Key Laboratory of Synthetical Automation for Process Industries, Northeastern University, Shenyang 110819, China*
[3]*School of Mechanical Engineering and Automation, Northeastern University, Shenyang 110819, China*

Correspondence should be addressed to Jianchang Liu; liujianchang@mail.neu.edu.cn

Received 6 December 2021; Accepted 27 December 2021; Published 18 January 2022

Academic Editor: Ahmed Mostafa Khalil

For personal safety and crime prevention, some research studies based on deep learning have achieved success in the object detection of X-ray security inspection. However, the research on dangerous liquid detection is still scarce, and most research studies are focused on the detection of some prohibited and common items. In this paper, a lightweight dangerous liquid detection method based on the Depthwise Separable convolution for X-ray security inspection is proposed. Firstly, a dataset of seven common dangerous liquids with multiple postures in two detection environments is established. Secondly, we propose a novel detection framework using the dual-energy X-ray data instead of pseudocolor images as the objects to be detected, which improves the detection accuracy and realizes the parallel operation of detection and imaging. Thirdly, in order to ensure the detection accuracy and reduce the computational consumption and the number of parameters, based on the Depthwise Separable convolution and the Squeeze-and-Excitation block, a lightweight object location network and a lightweight dangerous liquid classification network are designed as the backbone networks of our method to achieve the location and classification of the dangerous liquids, respectively. Finally, a semiautomatic labeling method is proposed to improve the efficiency of data labeling. Compared with the existing methods, the experimental results demonstrate that our method has better performance and wider applicability.

1. Introduction

At present, nondestructive testing technology has been widely applied in various fields [1–4], among which the application of X-ray detection technology in airports, customs, railway stations, and other transportation departments reduces criminal behavior effectively. However, the technology requires security inspectors to determine whether prohibited items are hidden in baggage. During the rush hours, the passing frequency of baggage increases greatly, and the security inspectors have to complete the detection in a very short time. Moreover, the images of prohibited items are often distorted or corrupted. These factors make detection more difficult and bring great challenges to security detection. Up to now, manual detection has been widely used in the field of X-ray security detection, but this method mainly relies on the experience of security inspectors. Meanwhile, the detection results of different security inspectors are also different. The accuracy of manual detection cannot be assured [5]. Accordingly, a fast and effective automatic object detection method for X-ray security inspection is significant.

In the early stage of the automatic object detection method for X-ray security inspection, some feature extraction algorithms are often used. Common feature extraction algorithms include Scale-invariant Feature Transform (SIFT), Histogram of Oriented Gradient (HOG), Haar-like features (Haar), etc. [6]. In addition, for the single-energy X-ray image, a method using the visual vocabulary and an occurrence structure generated from a training dataset were proposed in [7]. A new approach called Adaptive Sparse Representation (XASR+) was proposed in [8], and several patches were extracted from X-ray images to construct representative dictionaries in this method. For the

dual-energy X-ray pseudocolor images, Franzel et al. [9] used the visual vocabulary and the SVM classifier to detect handguns in hand luggage. Wang [10] et al. proposed a method by combining the Taruma feature based on the contourlet transform and the histogram, which applied the random forests classifier to classify these features from the illegal objects. In [11], Uroukov et al. used textural signatures to recognize and characterize materials. However, due to the wide variety of objects in X-ray security inspection, the fast detection requirement, the noise, the perspective imaging, the geometric distortion, and the objects placed closely together, these detection methods based on these manual features are not satisfactory.

In recent years, deep learning in image analysis and processing, especially the convolutional neural networks (CNNs), has achieved great success [12–14]. Compared with the manual feature extraction algorithms, the methods based on deep learning could automatically provide the most descriptive and differentiated features for each classification by training on a large dataset for a long time. For the object detection of natural optical images based on the convolutional neural network, the methods are mainly divided into two classifications. One is the two-stage method, such as R-CNN [15], Fast R-CNN [16], Faster RCNN [17], R-FCN [18], and FPN [19]. Such methods generate a set of candidate region suggestions firstly, and these candidates are classified, filtrated, and refined again. So far, the accuracy of the two-stage method still has been the highest among the object detection methods. The other is the one-stage method that directly predicts the classification and bounding box by a single convolutional network, such as YOLO methods [20–23] and SSD [24]. This kind of method has a faster detection speed, but the accuracy is lower than the two-stage method. Both of them have achieved brilliant achievements in the object detection of natural optical images and have been applied in various fields [25–27].

Compared with natural optical images, object detection in X-ray security inspection is still a huge challenge since X-ray images are very different from natural optical images. In [28], Mery et al. used transfer learning to classify three kinds of threat objects based on X-ray images and compared the experimental results with traditional computer vision methods. The experimental results showed that the X-ray image classification method based on deep learning is effective and potential. Akcay et al. [29] tested and evaluated several existing networks and object detection methods for six classifications of objects based on X-ray images, and the result showed the object detection methods with deep learning are better than the methods without deep learning. In [30], the researchers proposed a method that is more accurate and robust when dealing with the dense cluttered background in X-ray security inspection. The method adopted a specific data enhancement technique, the feature enhancement modules, and the multiscale fusion regions of interest (ROI). However, the current researches focused on a few common types of prohibited items due to the difficulty of establishing and extending a complete dataset. In response to this question, Zhang et al. [31] proposed a method of X-ray prohibited items image generation using Generative Adversarial Networks (GANs). In [32], Zhu et al. proposed a method based on Cycle GAN to transform the item natural images into X-ray images. These methods provide a new research direction for dataset expansion and lay a foundation for more accurate object detection in X-ray security inspection. Meanwhile, the high hardware requirements of these methods based on deep learning also limit their application.

At present, most researches are focused on the detection of some prohibited and common items, such as guns, knives, batteries, laptops, and bottles. The shapes and materials of these items are diverse. The above researches have made some contributions to the object detection of these items. Due to the high similarity of liquid pseudocolor images, the above researches can only detect bottles, not liquid types. However, for some special security occasions, only detecting the bottle is not enough. In these occasions, it is necessary to detect whether the liquid is harmful or even detect the type of the liquid. As far as we know, there is no research using dual-energy X-ray data to detect dangerous liquids. A possible solution to the classification of dangerous liquids is Energy dispersive X-ray diffraction (EDXRD). In [33], Zhong et al. found that Energy dispersive X-ray scattering profile is unique to each specific liquid material through experiments with three types of liquids. Tianyi et al. utilized EDXRD with hybrid discriminant analysis to classify the liquids in [34]. However, there are many problems in these researches. For instance, the sample must be a small dose, the container has specific requirements, the detection time is long, and the sample must be placed in a fixed position.

To solve these problems, we design an effective, lightweight dangerous liquid detection method, and it does not require high hardware requirements. The main contributions are as follows:

(i) We propose a novel framework using the dual-energy X-ray data instead of pseudocolor images as the objects to be detected, which improves the detection accuracy and realizes the parallel operation of detection and imaging

(ii) We design a lightweight object location network as the backbone network of object location, which ensures the object location accuracy and has fewer parameters and less computational consumption

(iii) We design a lightweight dangerous liquid classification network as the backbone network of classification, which has higher accuracy, fewer parameters, and less computational consumption

(iv) A dataset of seven common dangerous liquids containing multiple postures in two detection environments is established

(v) A semiautomatic labeling method is proposed to reduce the cost of manual labeling

The rest of the paper is organized as follows: Section 2 describes the creation and processing of the dataset. In Section 3, the proposed method is described. Section 4 presents the experiments and results. Finally, Section 5 concludes the paper and discusses some directions for future work.

2. Dataset

The dual-energy X-ray method has been widely used in X-ray security inspection systems [35]. In the method, the high-energy and low-energy data are converted into a pseudocolor image by a lookup table to facilitate the interpretation of the detected objects. In order for security inspectors to better distinguish the material of the detected object, orange represents organic matter, green represents mixture, and blue represents inorganic matter in the pseudo color image. In this paper, the dual-energy X-ray data used in this work are manually collected using X-ray security inspection equipment from Shenyang DT Inspection Equipment Co. Ltd. in China. The X-ray tube voltage and current are 140 kV and 0.75 mA, respectively. The X-ray security inspection equipment is shown in Figure 1. The value range of the dual-energy X-ray data is 0-15200. The size of each data is $600 \times 600 \times 2$.

A total of 7 kinds of dangerous liquids samples purchased from Sinopharm Chemical Reagents Shenyang Co., Ltd. without further purification are measured for our work. The samples are as follows: ethanol ($\geq 75\%$), ethanol ($\geq 95\%$, CP), methanol ($\geq 99.7\%$, GR), acetone (99.5%, AR), methylbenzene ($\geq 99.5\%$, AR), sulfuric acid (95–98%), and hydrochloric acid (36–38%). For descriptive convenience, the names of the liquids are substituted by chemical formulas in the latter part of this paper. Our X-ray dataset is divided into two parts to simulate two detection environments. One is to simulate the open-bag security inspection termed XD-O. This type of inspection is common in important situations such as airports. The other is to simulate the normal security inspection termed XD-N. For the XD-O, the samples with different postures are placed in the foam box and transferred to the security inspection machine through the conveyor belt. A total of 2318 dual-energy X-ray data are collected in the XD-O. For the XD-N, to simulate the real situation, the different baggage with the samples is packed and then sent into the security inspection machine. A total of 3596 dual-energy X-ray data are collected in the XD-N. The grayscale images of the dual-energy X-ray data are shown in Figure 2. The pseudo color images observed by the security inspectors are shown in Figure 3. Figure 4 shows the samples of the different liquids in the foam boxes and the real baggage.

From Figure 4, we can find that the similarity between sulfuric acid and hydrochloric acid is high and the other four liquids are also very similar under the conditions of our imaging method. Moreover, the pseudocolor images of these liquids may be more similar under the different levels of obscuration of different items. Considering this situation, it is difficult for the conventional algorithms based on the pseudocolor images to achieve the detection of these liquids. Therefore, our method uses the dual-energy X-ray data containing more detailed information instead of the pseudo color images as the objects to be detected. As a crucial part of the training network process, the dataset will directly affect the performance of deep learning methods. In order to improve the accuracy and robustness of our method, our dataset was augmented to 17308 samples by the translation, replication, and random noise injection.

3. Methods

In this section, the method proposed in this paper is described in detail. It is well known that some object detection methods, such as YOLO methods and Faster RCNN, are applied to various object detection tasks. However, the number of parameters and computational consumption is large for our detection task. In order to achieve a good balance between the number of parameters, computational consumption, and detection accuracy for our detection task, we propose a lightweight dangerous liquid detection method for X-ray security inspection (DLDX) with higher accuracy, fewer parameters, and less computational consumption. Firstly, we design the framework of the DLDX. Secondly, we design two lightweight networks as the backbone networks of the DLDX to achieve the object location and classification, respectively. Then, we design a semiautomatic labeling method for our dataset to improve the efficiency of data labeling. Finally, we give the training strategy of the DLDX.

3.1. The Framework of the DLDX. Our DLDX is designed based on the two-stage method. For the existing two-stage detection method, the candidate region suggestions are generated by the specific pooling operation (such as Roipooling and Roialign) on the candidate areas of the feature map, and then these candidates are classified, filtrated, and refined again. Although this approach is successful in the object detection of natural images, it causes a large amount of information loss in the process of object extraction, which is unfavorable to the dangerous liquid detection. At the same time, a large number of candidates also bring a large amount of computational consumption, which limits the application of this method.

To solve these problems, we propose the DLDX. The dual-energy X-ray data are used instead of pseudocolor images as the objects to be detected in the DLDX, which improves the detection accuracy and realizes the parallel operation of detection and imaging. The detection process is mainly divided into three parts: object localization, object extraction, and classification. Firstly, an object location network is used to precisely locate dangerous liquids. Secondly, to ensure the integrity of the extracted objects information, the objects are directly extracted from the dual-energy X-ray data through the position information of the objects output by the lightweight object location network, instead of extracting the objects on the feature map like the Roipooling and the Roialign. Then, in order to improve the classification accuracy, the extracted objects are padded to a fixed size. Considering the distance between the objects, the size of the objects, and the rationality of the network design, we use 15200 to pad the extracted objects to 256×192 instead of directly extracting the data with the size of 256×192 from the dual-energy X-ray data. Thirdly, these padded data are classified through a dangerous liquid classification network. Eventually, a pseudocolor image with the detection result is presented to the security inspectors. The overall architecture of the proposed method is shown in Figure 5.

(a) (b)

Figure 1: (a) The X-ray security inspection equipment. (b) The control station.

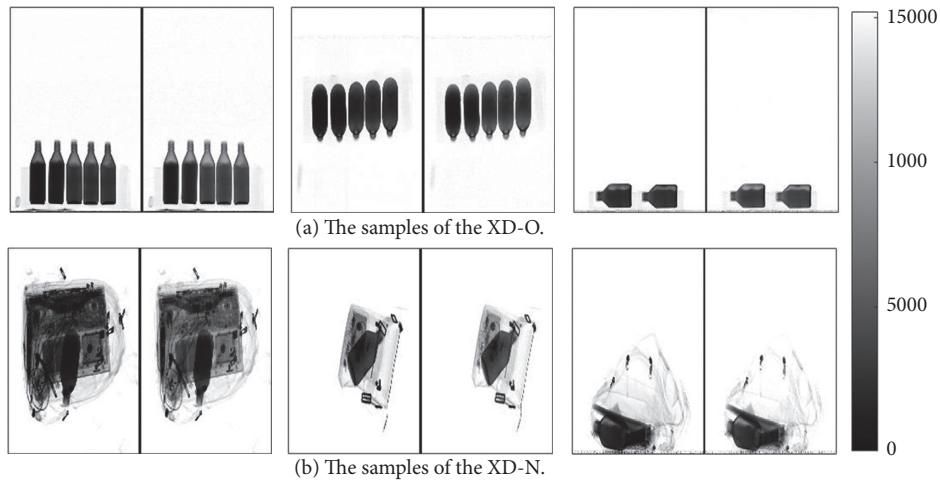

(a) The samples of the XD-O.

(b) The samples of the XD-N.

Figure 2: Some grayscale images of the dual-energy X-ray data. (The left side of each image is the low-energy image and the right side is the high-energy image.) (a) The sample of the XD-O. (b) The sample of the XD-N.

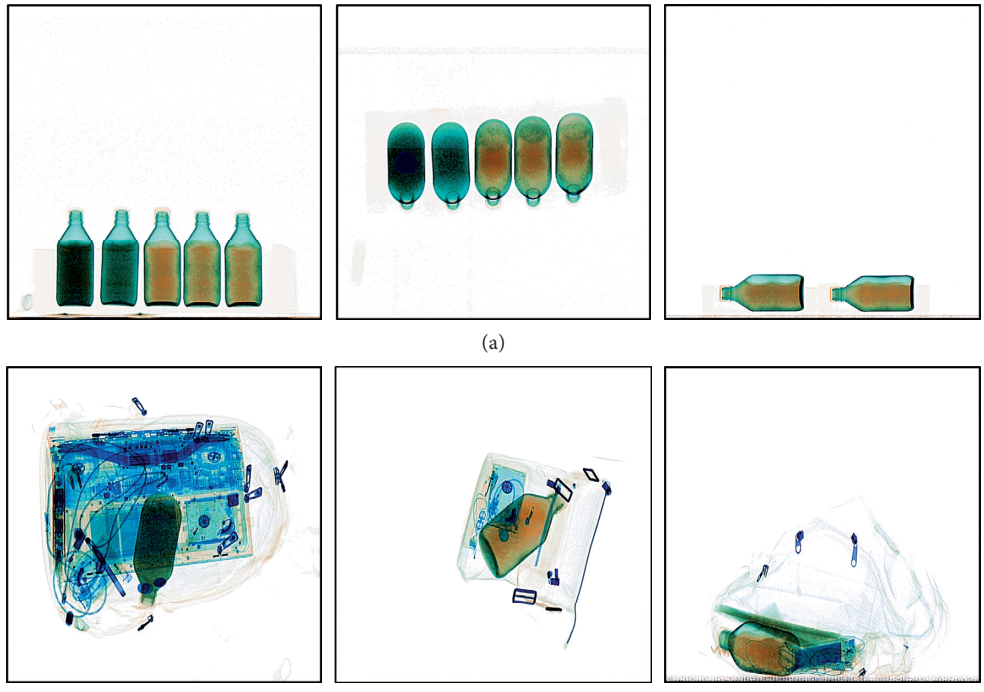

(a)

(b)

Figure 3: Some pseudocolor images of the dual-energy X-ray data. (a) The sample of the XD-O. (b) The sample of the XD-N.

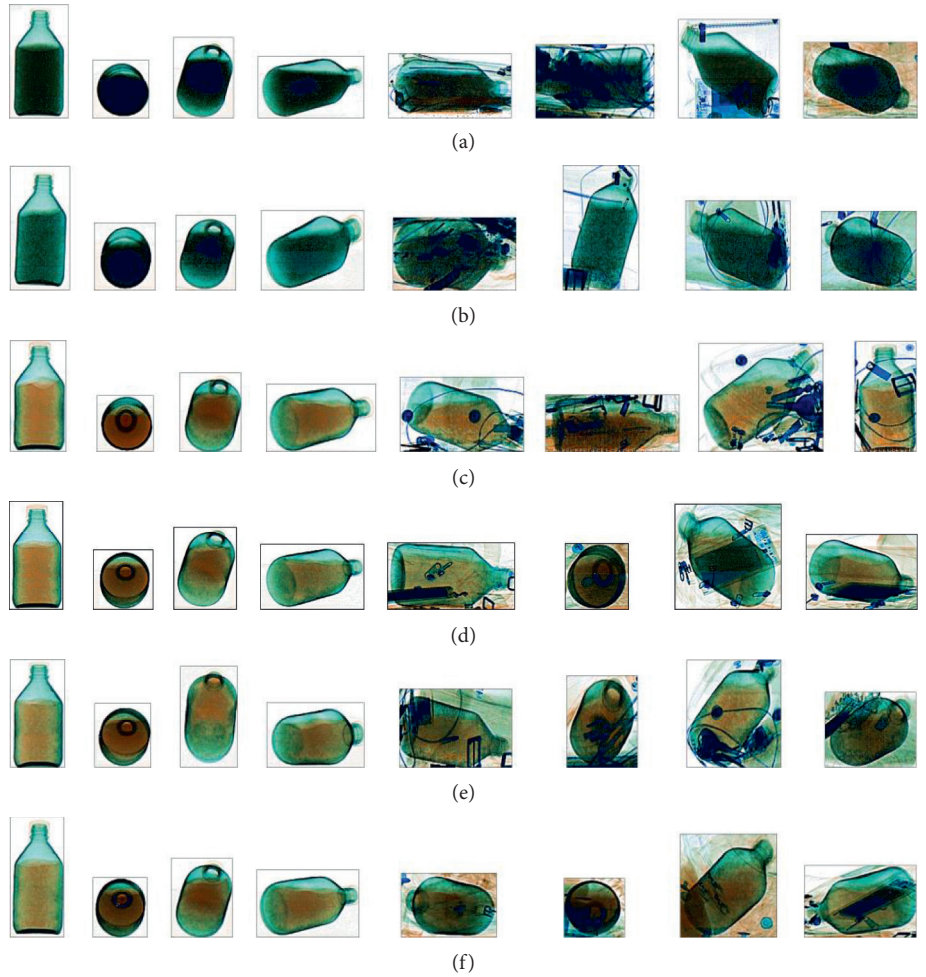

Figure 4: Some pseudocolor images of the different liquids. (a) Some samples of H2SO4. (b) Some samples of HCL. (c) Some samples of C7H8. (d) Some samples of CH3OH. (e) Some samples of CH3COCH3. (f) Some samples of C2H5OH.

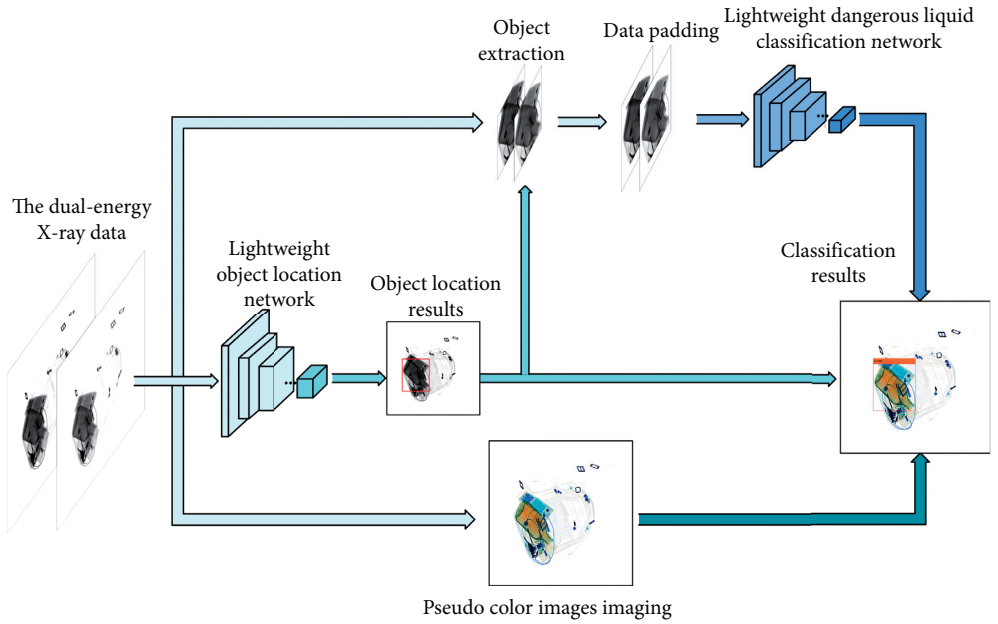

Figure 5: The framework of the DLDX.

3.2. A Lightweight Object Location Network. The design of the backbone network is significant for the accurate prediction of object locations. Therefore, this subsection focuses on developing a lightweight object location network of dangerous liquids that has both high detection accuracy and low computational cost. For the two-stage detection methods, taking Faster RCNN as an example, the Region Proposal Network (RPN) generates the candidate region suggestions with various scales and ratio aspects on the feature map to coarsely regress the bounding box location and classify the foreground and background. And then these candidates are fed into the next network to refine the bounding box location and classification accuracy. Finally, the bounding box coordinates, class labels, and classification accuracy are output. Although this method ensures detection accuracy, it also brings a large amount of calculation consumption due to the processing of a large number of candidates from the RPN. It is worth noting that the image data is three-dimensional with a value range of 0–255, while our data is two-dimensional with a value range of 0–15200. This means that our dataset is quite different from the ImageNet dataset and the fine-tuning of the networks pretrained on the ImageNet dataset is impossible. Meanwhile, designing a new network with lots of parameters makes training difficult and requires a huge dataset. Based on the above discussion, we design a lightweight object location network fitting our dual-energy X-ray dataset. It has fewer parameters and can be trained from scratch with our dataset.

In our lightweight object location network, the Depthwise Separable convolution composed of the Depthwise convolution (DWC) and the Pointwise convolution (PWC) is employed. The DWC is operated by channel-wise fashion and the PWC is the standard convolution with 1×1 kernels. The operation process of the Depthwise Separable convolution is shown in Figure 6. To illustrate the advantages of the Depthwise Separable convolution, we compare the Depthwise Separable convolution and the standard convolution in terms of the number of parameters (Params) and the number of multiply-accumulate operations (Madds).

Given an input feature map $X_{\text{in}} \in R^{H \times W \times C}$ and an output feature map $X_{\text{out}} \in R^{\widetilde{H} \times \widetilde{W} \times \widetilde{C}}$, the ratio of Madds between the Depthwise Separable convolution and the standard convolution can be represented as follows:

$$\begin{aligned} R_{\text{Madds}} &= \frac{\text{Madds}_{ds}}{\text{Madds}_{s}} \\ &= \frac{D_k \times D_k \times C \times \widetilde{H} \times \widetilde{W} + C \times \widetilde{C} \times \widetilde{H} \times \widetilde{W}}{D_k \times D_k \times C \times \widetilde{C} \times \widetilde{H} \times \widetilde{W}} \\ &= \frac{1}{\widetilde{C}} + \frac{1}{D_k \times D_k}, \end{aligned} \tag{1}$$

where D_k is the size of the convolution kernel, Madds_{ds} is the Madds of the Depthwise Separable convolution, and Madds_{s} is the Madds of the standard convolution. The ratio of Madds between the Depthwise Separable convolution and the standard convolution can be represented as follows:

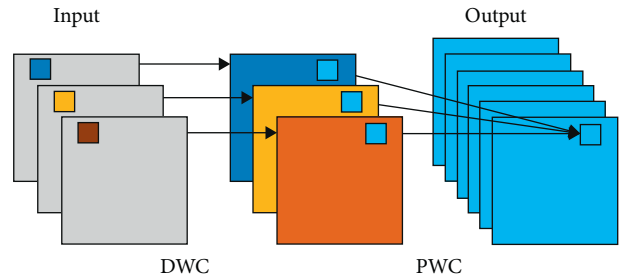

Figure 6: The convolution process of the Depthwise Separable convolution.

$$\begin{aligned} R_{\text{Params}} &= \frac{\text{Params}_{ds}}{\text{Params}_{s}} = \frac{D_k \times D_k \times C + C \times \widetilde{C}}{D_k \times D_k \times C \times \widetilde{C}} \\ &= \frac{1}{\widetilde{C}} + \frac{1}{D_k \times D_k}, \end{aligned} \tag{2}$$

where Params_{ds} is the Params of the Depthwise Separable convolution and Params_{s} is the Params of the standard convolution.

We can find the Params and Madds of the Depthwise Separable convolution have been greatly reduced. Based on the computational advantage of the Depthwise Separable convolution, it is employed in some successful lightweight networks, such as MobilenetV1 [36] and MobilenetV2 [37]. In MobilenetV2, the inverted residual block was proposed based on the DWC and the residual network. As the Depthwise convolution is operated by channel-wise fashion, the feature information can only be transferred in one channel. Meanwhile, the ReLu6 activation function causes a large amount of information loss in the inverted residual block. Therefore, we improve the inverted residual block in MobilenetV2, as shown in Figure 7. In the improved inverted residual (IIRS) block, we replace the ReLu6 activation function of the first PWC with the LeakyRelu and remove the activation functions after the DWC, which ensures the effective transmission of the information.

Our lightweight object location network is designed based on the IIRS block. The architecture of the lightweight object location network is shown in Table 1. First, a 3×3 Conv + BatchNormalization + LeakyRelu block is used to reduce the dimension of the input data and extract roughly the features. As the network needs to be trained from scratch, the use of the Batchnormalization and the LeakyRelu makes the training of the network easier. Then, four IIRS blocks are applied to extract the object features accurately with fewer parameters. Subsequently, in order to reduce the computational consumption, only two 3×3 Conv + BatchNormalization + LeakyRelu blocks are used to extract the features more accurately.

Next, we use the K-means clustering algorithm to obtain the size of the anchor boxes. A total of six anchor boxes are obtained for getting more precise object positions. It is well known that feature maps with the larger size contain richer location information. In order to make the prediction of the object location more accurate and take into account the computational consumption, the size of the feature map is

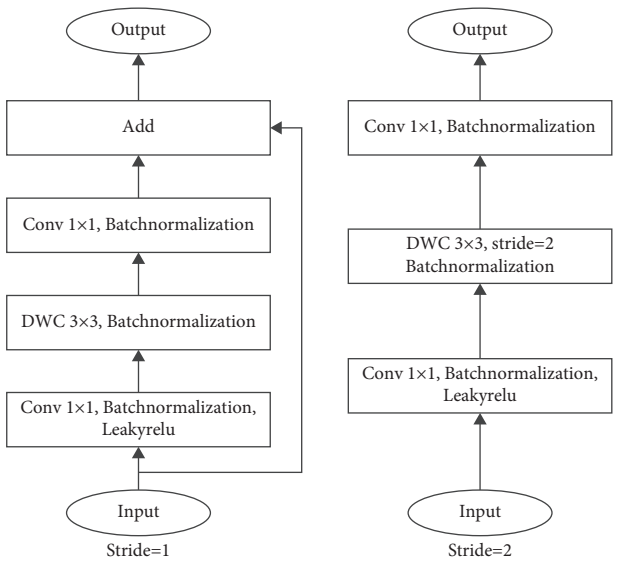

Figure 7: The structure of the improved inverted residual block.

Table 1: The architecture of the lightweight object location network.

Input	Operator	C	T	Stride
$600 \times 600 \times 2$	Conv + Bn + LeakyRelu	16	—	2
$300 \times 300 \times 16$	IIRS block	32	1	2
$150 \times 150 \times 32$	IIRS block	32	3	1
$150 \times 150 \times 32$	IIRS block	64	3	2
$75 \times 75 \times 64$	IIRS block	64	2	1
$75 \times 75 \times 64$	Conv + Bn + LeakyRelu	64	—	1
$75 \times 75 \times 64$	Conv + Bn + LeakyRelu	64	—	1
$75 \times 75 \times 64$	Conv	30	—	1
$75 \times 75 \times 30$	Sigmoid + Exp function	—	—	—
Output	$75 \times 75 \times 30$			

T is the multiplier of the input channel and C is the number of the last PWC channels.

set as 75×75. That is to say, the input data is divided into 75×75 grids. In each grid, the prediction information from the last convolutional layer consists of the position offset (t_x, t_y), width offset t_w, height offset t_h and confidence score p of each anchor box. Using the sigmoid and exp function, we can obtain the final output $(t_{fx}, t_{fy}, t_{fw}, t_{fh}, p_f) = (S(t_x), S(t_x), e^{t_w}, e^{t_h}, S(p))$, where $S(\cdot)$ is the sigmoid function and e is the natural logarithm. The actual coordinates (x, y, w, h) and the normalized confidence score P can be obtained through the following equation:

$$\begin{bmatrix} x \\ y \\ w \\ h \\ P \end{bmatrix} = \begin{bmatrix} \left(t_{fx} + c_x\right) \times F \\ \left(t_{fy} + c_y\right) \times F \\ A_w \times t_{fw} \\ A_h \times t_{fh} \\ p_f \end{bmatrix}, \tag{3}$$

where F is the minification factor of the feature map, $F = 600/75$ (600 is the input size and 75 is the feature map size) in this paper, (c_x, c_y) is the coordinate in the upper left corner of each grid in the feature map, (A_w, A_h) is the width and height of the anchors.

At the end of the lightweight object location network, multiple overlapping candidate boxes will be suggested, and we must choose the best one from these candidate boxes for each object. Therefore, Soft-NMS algorithm [38] is used to update the score of each boundary box. Define $B = \{b_1, b_2, \ldots, b_N\}$ as the set of the candidate boxes and $V = \{v_1, v_2, \ldots, v_N\}$ as the corresponding set of the scores. The choice criterion in Soft-NMS can be written as follows:

$$V_i = \begin{cases} V_i, & \mathrm{IOU}\left(b_m, b_i\right) < T, \\ V_i\left(1 - \mathrm{IOU}\left(b_m, b_i\right)\right), & \mathrm{IOU}\left(b_m, b_i\right) \geq T, \end{cases} \tag{4}$$

where b_m is the candidate box which has the highest score, b_i is the initial detection candidate box, and T is the threshold value of the intersection over union (IOU). IOU is the ratio of the intersection and union of two candidate boxes. When the IOU values of the candidate boxes are smaller than the threshold T, the scores of the candidate boxes remain unchanged. Soft-NMS assigns lower scores to the neighboring candidate boxes, whose IOU values are bigger than the threshold T until the final prediction boxes are selected instead of removing them.

The loss function of the lightweight object location network L_{object} consists of the coordinate error L_{boxes} and the confidence score error L_{score}. The coordinate error can be defined as follows:

$$\begin{aligned} L_{\text{boxes}} = \lambda_{\text{cood}} \sum_{i=1}^{M} \sum_{j=1}^{N} I_{ij}^{obj} \Big[& \left(t_{fxij} - \hat{t}_{fxij}\right)^2 + \left(t_{fyij} - \hat{t}_{fyij}\right)^2 \\ & + \left(t_{fwij} - \hat{t}_{fwij}\right)^2 + \left(t_{fhij} - \hat{t}_{f}hij\right)^2 \Big], \end{aligned} \tag{5}$$

the confidence score error is defined as follows:

$$\begin{aligned} L_{\text{score}} = & -\sum_{i=1}^{M} \sum_{j=1}^{N} I_{ij}^{obj} \lambda_{obj} \left(p_{fi} - \hat{p}_{fi}\right)^2 \\ & + \lambda_{\text{noobj}} \sum_{i=1}^{M^2} \sum_{j=1}^{N} I_{\text{IOU<Thresh}} \left(p_{fi}\right)^2, \end{aligned} \tag{6}$$

and the final loss function can be expressed as follows:

$$L_{\text{object}} = L_{\text{boxes}} + L_{\text{score}}, \tag{7}$$

where λ_{cood} is the weight coefficient of the coordinate error (set as 1), λ_{obj} is the weight coefficient of the confidence error for the grids with an object (set as 5), λ_{noobj} is the weight coefficient of the confidence error for the grids with the IOU less than the threshold (set as 0.5), M is the number of the grids (set as 75×75), N is the number of the anchor boxes in each gird (set as 6), $(\hat{t}_{fxij}, \hat{t}_{fyij}, \hat{t}_{fwij}, \hat{t}_{fhij}, \hat{p}_{fij})$ is the true value for $(t_{fxij}, t_{fyij}, t_{fwij}, t_{fhij}, p_{fij})$, I_{ij}^{obj} is 1 if the j th anchor box predicted by grid i is responsible for the prediction (0 otherwise), and $I_{\text{MaxIOU<Thresh}}$ is 1 if the IOU of the j th anchor box predicted by grid i is less than the threshold (0 otherwise).

3.3. A Lightweight Dangerous Liquid Classification Network. After the object location and the data padding, these padded data are classified through a dangerous liquid classification network in our DLDX. The design of the classification network is very significant and it directly affects the performance of our DLDX. At present, some public CNN networks can be used for the image feature extraction, such as Darknet [20, 21], Resnet [14], MobilenetV2 [37], MobilenetV3 [39], and SqueezeNet [40]. These networks have outstanding performance in the object detection of natural images, and they are usually used as the backbone networks for feature extraction when dealing with practical problems in the engineering field. Meanwhile, transfer learning is often adopted to solve these problems. However, transfer learning is not applicable for our dataset because our dataset is completely different from the ImageNet dataset. In order to ensure the accuracy of the classification and reduce the computational consumption and the number of parameters, we designed our lightweight dangerous liquid classification network based on the IIRS block and the Squeeze-and-Excitation (SE) block [41].

The SE block can be understood as feature maps recalibrated according to channels. This recalibration makes the network ignore those channels with less meaningful information and focus on the ones that provide more meaningful information. The structure of the SE block is shown in Figure 8. Given an input feature map $X \in R^{H\times W\times C}$, we can get the recalibrated feature map $\widetilde{X} \in R^{H\times W\times C}$ through the SE block. X and $\widetilde{X}$ can be expressed as $X = [x_1, x_2, \ldots, x_C]$ and $\widetilde{X} = [\widetilde{x}_1, \widetilde{x}_2, \ldots, \widetilde{x}_C]$. Firstly, the global average pooling is used to generate a $1 \times 1 \times C$ feature map $O = [o_1, o_2, \ldots, o_C]$ to express X in general. This process can be expressed as follows:

$$O_k = \frac{1}{H \times W} \sum_{i=1}^{H} \sum_{j=1}^{W} x_k(i, j), \quad k = 1, 2, \ldots, C. \tag{8}$$

Secondly, the channel-wise dependencies $\widetilde{O} = [\widetilde{o}_1, \widetilde{o}_2, \ldots, \widetilde{o}_C]$ are extracted using fully connected (FC) layers and nonlinearity layers. The connection mode is shown in Figure 8. We can obtain the following:

$$\widetilde{O} = S(\mathbf{W}_2 \sigma(\mathbf{W}_1 O)), \tag{9}$$

where σ represents the Relu activation function, $\mathbf{W}_1 \in R^{(C/r)\times C}$ and $\mathbf{W}_2 \in R^{C\times(C/r)}$ are the weights of the fully connected layers, r is a ratio parameter. Finally, the recalibrated feature map $\widetilde{X}$ can be obtained by the following equation:

$$\widetilde{X} = \text{Scale}(\widetilde{O}, X) = [\widetilde{o}_1 x_1, \widetilde{o}_2 x_2, \ldots, \widetilde{o}_C x_C], \tag{10}$$

where $\text{Scale}(\cdot)$ refers to channel-wise multiplication between the scalar $\widetilde{O}$ and the feature map X.

Following, we combine the IIRS block and the SE block into an IIRS + SE block. The SE block is placed behind the last PWC in the IIRS + SE block. This approach can recalibrate the information of the IIRS block better. The structure of the IIRS + SE block is shown in Figure 9. Table 2 shows the architecture of our lightweight dangerous liquid classification network.

First, like the lightweight object location network, a 3×3 Conv + BatchNormalization + LeakyRelu block is used to reduce the dimension of the input data and extract the features roughly. Second, on the premise of effectively extracting features, in order to reduce the computational consumption and the difficulty of network training, the IIRS + SE blocks with stride = 1 and stride = 2 are combined, as shown in Table 2. After the last IIRS + SE block, a 1×1 convolution filter is adopted to increase the dimension and enrich the information of the extracted feature. And then, the average global pooling is adopted to reduce computational consumption and prevent overfitting, like most networks. Finally, full connection and softmax are used to output the final classification results. We use the cross entropy function as the loss function:

$$L_{\text{class}} = -\sum_{k=1}^{K} \widehat{P}_{ck} \log(P_{ck}), \tag{11}$$

where K is the number of classes, $\widehat{P}_{ck}$ is the actual label of the input data, and P_{ck} is the probability that the Softmax layer predicts the input data belonging to the class k.

3.4. A Semiautomatic Labeling Method. Information labeling is the basis of building deep learning models and a necessary process for supervised machine learning algorithms. For the public datasets, the most common labeling method is manually labeled by the crowdsourcing business model. However, the datasets in the security field are highly professional and confidential and cannot be transmitted via the Internet. This leads to a significant increase in the cost of manual labeling. In order to reduce the cost of manual labeling of our dangerous liquid dataset, a semiautomatic labeling method based on active learning is designed to improve the efficiency of dataset labeling, and the lightweight object location network is fine-tuned in the process.

To introduce our algorithm clearly, the augmented dual-energy X-ray dataset is defined as $U = \{U_1, U_2\}$, where U_1 is the labeled dataset, $U_2 = \{\widetilde{U}_1, \widetilde{U}_2, \ldots, \widetilde{U}_n\}$ is the dataset with classification labels but without location labels, and it is divided into n datasets to be labeled. The semiautomatic labeling algorithm is shown in Algorithm 1.

In our semiautomatic labeling method, the initial state of the dual-energy X-ray dataset with labels $\overline{U}$ is U_1. Next, the initialized object location network is trained on the labeled dataset U_1, and the trained object location network is used to predict the subset in U_2. For each subset of U_2, the samples with low confidence and the undetected samples are selected and put into the manually labeled dataset U_m, and the samples with high confidence are updated with the labels of the prediction. In the end, the manually labeled dataset and updated dataset are combined into $\overline{U}$ for fine-tuning the object location network until all subsets of U_2 are processed.

3.5. Training Strategy of the DLDX. For our DLDX, two networks need to be trained. The object localization network can be trained in the semiautomatic labeling process and can also be directly trained by using the labeled dataset. After

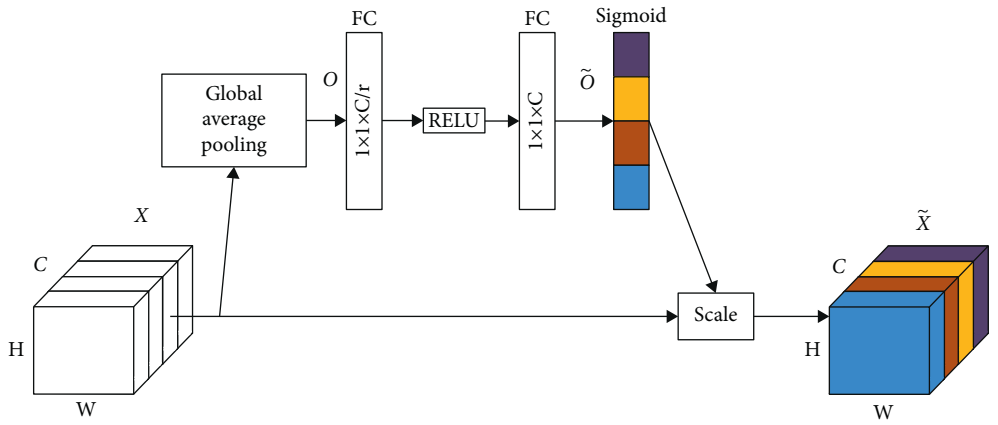

Figure 8: The structure of the Squeeze-and-Excitation block.

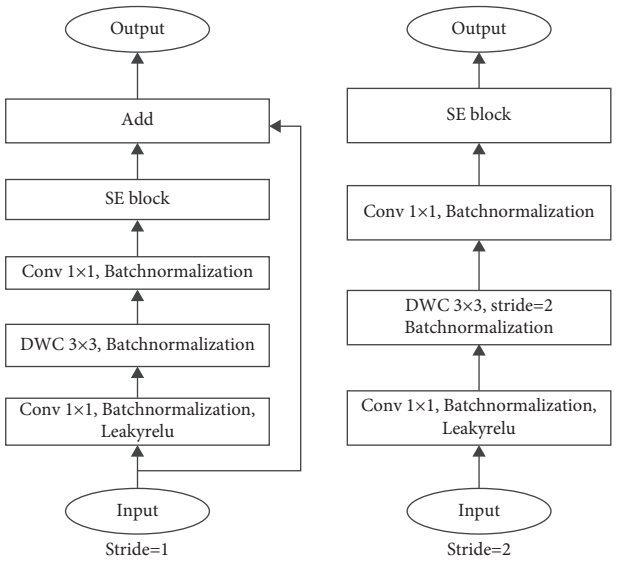

Figure 9: The structure of the IIRS + SE block.

Table 2: The architecture of the lightweight dangerous liquid classification network.

Input	Operator	C	T	Stride	r
$256 \times 192 \times 2$	Conv + Bn + LeakyRelu	16	—	2	—
$128 \times 96 \times 16$	IIRS + SE block	16	2	2	16
$64 \times 48 \times 16$	IIRS + SE block	16	3	1	16
$64 \times 48 \times 16$	IIRS + SE block	32	3	2	16
$32 \times 24 \times 32$	IIRS + SE block	32	3	1	16
$32 \times 24 \times 32$	IIRS + SE block	64	3	2	16
$16 \times 12 \times 64$	IIRS + SE block	64	3	1	16
$16 \times 12 \times 64$	IRS + SE block	128	3	2	16
$8 \times 6 \times 128$	IRS + SE block	128	4	1	16
$8 \times 6 \times 128$	Conv + Bn + LeakyRelu	512	—	1	—
$8 \times 6 \times 512$	Globalpooling	—	—	—	—
$1 \times 1 \times 512$	Fully connected	6	—	—	—
Output	Softmax				

training the object localization network, the trained object localization network is used to extract the dangerous liquid objects from the dual-energy X-ray dataset as the training dataset of the dangerous liquid classification network. In the extraction process, the object location network outputs the bounding boxes after shielding the Soft-NMS algorithm. Then the IOU values of the generated bounding boxes and corresponding labeled boxes are calculated and sorted, and up to 10 bounding boxes are selected for each object. These extracted objects are padded to 256×192 to form the training dataset of the dangerous liquid classification network. Finally, the dangerous liquid classification network can be trained on the dataset.

4. Experimental Results and Analyses

In this section, we first test our semiautomatic labeling method, then compare our DLDX with the existing methods and analyze the experimental results. The experiments are run on a GPU system with the following specifications: Intel Core i9-10900k CPU, 64 GB RAM and NVIDIA GeForce GTX 3090 GPU.

4.1. Evaluation Criteria. In this paper, average precision (AP) and mean average precision (*mAP*) are used to evaluate the performance of the methods. In addition, *m*IOU is the average of the IOU values of all predicted boxes and object boxes, and it is also used to evaluate the methods. Precision and Recall are calculated using the following equations:

$$\mathrm{Pr} = \frac{\mathrm{TP}}{\mathrm{TP} + \mathrm{FP}}, \tag{12}$$

$$\mathrm{Re} = \frac{\mathrm{TP}}{\mathrm{TP} + \mathrm{FN}}, \tag{13}$$

where TP is the number of true positive samples, FP is the number of false-positive samples, and FN is the number of false-negative samples. High precision indicates high accuracy of detection results, and high Recall means fewer missed objects in the detection process. Average precision can be calculated as follows:

$$\mathrm{AP} = \frac{1}{11} \sum_{\mathrm{Re} \in \{0, 0.1, 0.2, \ldots\ldots, 1\}} \max_{\widetilde{\mathrm{Re}}:\ \widetilde{\mathrm{Re}} \geq \mathrm{Re}} \mathrm{Pr}(\widetilde{\mathrm{Re}}), \tag{14}$$

where $\mathrm{Pr}(\mathrm{Re})$ is the measured precision at recall Re. Subsequently, *mAP* can be defined as follows:

Input: The dual-energy X-ray dataset, U the lightweight object location network N_{obj} and the confidence score threshold T
Output: The dual-energy X-ray dataset with labels $\widetilde{U}$ and the trained lightweight object location network N_{obj}

Train N_{obj} with U_1
$\overline{U} = U_1$
For $i = 1$, $i \leq n$, i++ **do** predict $\widetilde{U}_i$ with N_{obj}, get confidence score P_i and Location L_i;
  For $C_j \in \widetilde{U}_i$ **do**
    If $P_j < T$ or manually verify the existence of undetected object **then**
      Remove C_j into U_m;
      Delete the corresponding object information;
    Else
      Update the labels of C_j;
    End if
  End for
  Label U_m manually;
  $\overline{U} = \overline{U} \cup U_m \cup \widetilde{U}_i$;
  Fine-tune N_{obj} with $\overline{U}$;
  Empty U_m;
End for
Return $\overline{U}$ and N_{obj};

Algorithm 1: Semiautomatic labeling method.

$$mAP = \frac{1}{K} \sum_{k=1}^{K} AP_k. \tag{15}$$

4.2. Results and Discussion. In order to verify the effectiveness of our semiautomatic labeling method, we manually labeled our dataset and randomly selected some data to form the unlabeled dataset. Then, we used our semiautomatic labeling method to train our lightweight object location network and label the unlabeled dual-energy X-ray dataset. In the process, U_1 contained 8440 samples, U_2 was divided into four subsets (each subset contained 2000 examples), and the confidence score threshold T was set as 0.9. Adaptive moment estimation (Adam) optimization algorithm was used for the training of all networks and the batch size was 8. For U_1, the initial learning rate was 0.001, the exponential decay rate for the first moment estimate was 0.9, the exponential decay rate for the second moment estimate was 0.999, and the max epoch was 100. For the process of fine-tuning, the learning rate was 0.0001, the max epoch was 20, and other parameters were the same as above. Meanwhile, we also trained our lightweight object location network on the manually labeled dataset for comparison with our method. The results are given in Table 3. The results show the *mIOU* of the trained lightweight object location network with our semiautomatic labeling is only 0.011 lower than the network trained on manually labeled dataset. The small gap is entirely acceptable. Therefore, our semiautomatic labeling method is effective.

Table 3: The object location results.

Method	MIOU	AP
Semiautomatic labeling	0.878	100
Manually labeled dataset	**0.889**	100

And then, we prioritized training our DLDX on the XD-O. The samples in the XD-O all have simple backgrounds and the training results can better represent the feature extraction and classification abilities of our DLDX for the different liquids. In the process, Adam optimization algorithm was used. The batch size was 64, the max epoch was 30, the initial learning rate was 0.001, and other parameters were the same as above. Moreover, to further evaluate the performance of our method, we also trained the existing object detection methods and the existing lightweight CNN networks as the backbone networks of the DLDX to compare with our DLDX. Considering the existing methods were designed based on images, we converted the XD-O into a corresponding pseudocolor images dataset and trained the existing methods on the XD-O and the pseudocolor images dataset. The detection results of each method are shown in Table 4.

Meanwhile, in order to compare the complexity of each method, the Params and Madds of each method are shown in Table 5. As the Params and Madds of Faster RCNN are much more than others, they are not given in Table 5. In addition, the Params and Madds of the method based on the dual-energy X-ray dataset and pseudocolor images dataset are almost equal. Therefore, only the Params and Madds of the methods based on the dual-energy X-ray data are given in Table 5.

From Table 4, we can find that the *mAP* of the methods using the dual-energy X-ray data as the input is generally better than the methods using the pseudocolor images as input. This proves that it is reliable for using the dual-energy X-ray data as the objects to be detected. In terms of the structures of the methods, using the same backbone network, the *mAP* and the *mIOU* of our DLDX are higher than those of YOLOV4_tiny and Faster RCNN. It is worth noting that compared with using YOLOV4_tiny, the Params of using the DLDX are reduced by 45% for mobileNetV2 and

Table 4: The detection results of the different methods on the XD-O.

Method	MIOU	MAP (%)	AP(%)					
			H2SO4	HCL	C7H8	CH3OH	CH3COCH3	C2H5OH
YOLOV 4_tiny_X-ray	0.892	94.34	**100**	**100**	92.84	89.66	92.40	91.16
YOLOV4_tiny_MobileNetV2_X-ray	0.884	93.78	**100**	**100**	90.06	92.93	90.62	89.06
YOLOV4_tiny_MobileNetV3_X-ray	0.884	94.33	**100**	99.22	92.19	88.83	93.75	91.97
YOLOV4_tiny_image	0.892	92.68	98.44	96.88	91.28	91.41	89.80	88.24
YOLOV4_tiny_MobileNetV2_image	0.884	91.74	95.12	**100**	91.39	89.02	82.88	92.04
YOLOV4_tiny_MobileNetV3_image	0.885	92.38	93.75	98.44	92.19	86.72	89.70	93.48
FasterRCNN_MobileNetV2_X-ray	0.819	91.92	91.95	98.99	88.28	92.44	87.49	92.37
FasterRCNN_MobileNetV3_X-ray	0.821	92.03	91.35	98.44	92.19	90.59	86.72	92.88
FasterRCNN_MobileNetV2_image	0.821	89.95	92.91	98.44	86.67	88.25	85.91	87.49
FasterRCNN_MobileNetV3_image	0.822	90.73	93.75	98.44	92.13	85.12	86.64	88.27
DLDX_MobileNetV2	**0.902**	98.05	**100**	99.22	90.63	**100**	**98.44**	**100**
DLDX_MobileNetV3	**0.902**	97.43	**100**	**100**	90.24	99.82	96.88	97.66
DLDX	**0.902**	**98.28**	**100**	**100**	**96.02**	99.88	96.88	96.88

Table 5: The Params and Madds of the different methods.

Method	Params (m)	Madds
YOLOV4_tiny	5.9	7144 m
YOLOV4_tiny_MobileNetV2	4.3	3477 m
YOLOV4_tiny_MobileNetV3	3.4	2832 m
DLDX_MobileNetV2	2.4	$856\,m + 290\,m \times n$
DLDX_MobileNetV3	2.8	$856\,m + 195\,m \times n$
DLDX	0.4	$856\,m + 50\,m \times n$

m denotes million and n is the number of objects.

20% for mobileNetV3. Since our DLDX classifies objects after locating them, the Madds of the DLDX is related to the number of objects. For the DLDX with mobileNetV2 and mobileNetV3, their Madds are the same as using YOLOV4_tiny when each sample contains ten objects, the Madds are reduced by 50% when each sample contains three objects and the Madds are reduced by 67% when each sample contains one object. In terms of the backbone networks, the *mAP* of the DLDX with mobileNetV2 and mobileNetV3 is almost equal to our method, but the Params of our method are reduced by about 80%. Compared with mobileNetV2 and mobileNetV3, the Madds of our lightweight dangerous liquid classification network is reduced by 74% and 83%, respectively. According to the above analysis, it can be concluded that our DLDX can accomplish highly accurate dangerous liquid detection in the open-bag security inspection and the fewer Params and Madds of our DLDX can also greatly reduce the hardware requirements, which makes our DLDX have wider applicability.

To further verify the performance of our DLDX in complex environments, we trained our DLDX on the XD-N. According to the experimental results based on the XD-O, YOLOV4_tiny_MobileNetV2_X-ray, YOLOV4_tiny_MobileNetV3_X-ray, DLDX_MobileNetV2, and DLDX_MobileNetV3 were selected to compare with our DLDX. The detection results are shown in Table 6. From Table 6, we can find that the *mAP* and the *m*IOU of these methods decrease on the XD-N with complex background. However, the *mAP* of our DLDX is still able to reach 90.96%, and using the same backbone network, the *mAP* and the *m*IOU of our DLDX is higher than those of YOLOV4_tiny. Among these methods, our DLDX still has the highest *m*IOU and *mAP*, although the AP of HCL, CH3OH, CH3COCH3, and C2H5OH are slightly lower than that of the DLDX using MobileNetV2 and MobileNetV3 as backbone networks.

Except that, we adopted the t-distributed stochastic neighbor embedding method (t-SNE) [42] as the feature visualization method to demonstrate the feature extraction ability of our method. The results are shown in Figure 10. The visualization results indicate that our method can extract better features from the samples with simple backgrounds in the open-bag security inspection to distinguish the different liquid classes. The quality of the extracted features for the samples with complex backgrounds is slightly inferior to that of the samples with simple backgrounds, which is the reason for the decrease in the accuracy of identifying the samples with complex backgrounds. According to the above analysis, it can be concluded that our method is more suitable for the detection of dangerous liquids and has wider applicability than other methods.

Table 6: The detection results of the different methods on the XD-N.

Method	MIOU	MAP (%)	AP(%)					
			H2SO4	HCL	C7H8	CH3OH	CH3COCH3	C2H5OH
YOLOV4_tiny_MobileNetV2_X-ray	0.824	83.75	97.62	90.89	68.71	83.63	73.91	87.73
YOLOV4_tiny_MobileNetV3_X-ray	0.835	84.12	95.18	90.91	66.44	88.03	75.24	88.89
DLDX_MobileNetV2	**0.876**	89.14	97.56	**94.86**	86.64	80.84	84.47	90.44
DLDX_MobileNetV3	**0.876**	90.56	**100**	92.80	84.14	**85.60**	**89.77**	**91.05**
DLDX	**0.876**	**90.96**	**100**	94.57	**88.03**	85.59	87.28	90.27

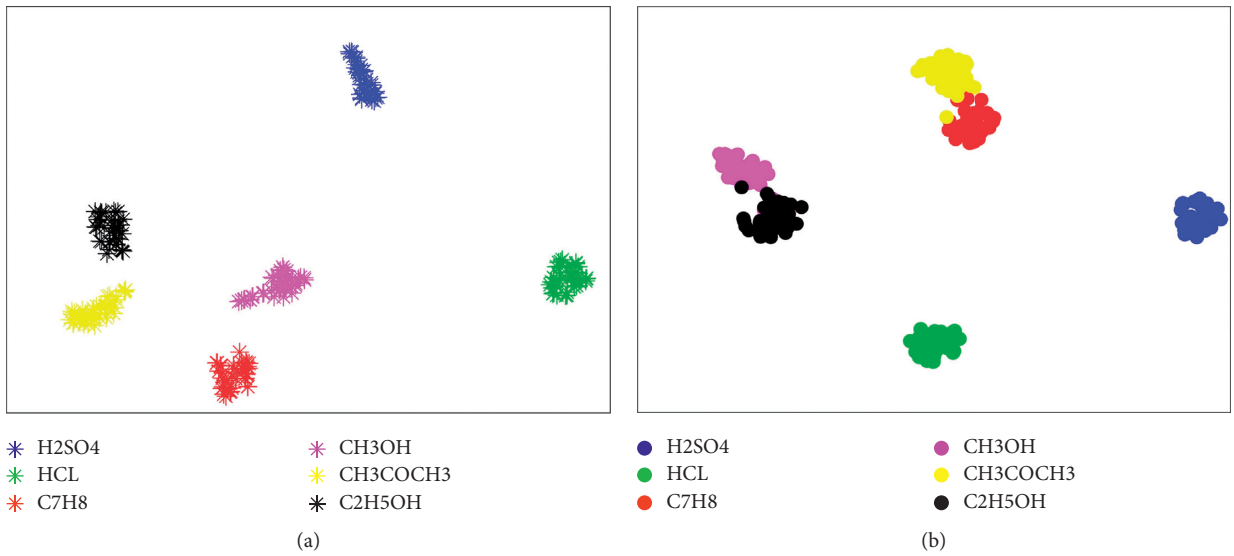

Figure 10: The feature visualization results based on t-SNE for our method. (a) XD-O. (b) XD-N.

5. Conclusion

In this paper, an effective lightweight, dangerous liquid detection method for X-ray security inspection termed DLDX is proposed. The innovation is mainly reflected in three major aspects. First, a novel detection framework using the dual-energy X-ray data as the objects to be detected is proposed to improve the detection accuracy and realize the parallel operation of detection and imaging. Different from the framework of existing two-stage methods, the objects are directly extracted from the dual-energy X-ray data and padded to a fixed size as candidates in our DLDX, which ensures the integrity of the information. Second, in order to ensure the detection accuracy and reduce the computational consumption and the number of parameters, a lightweight object location network and a lightweight dangerous liquid classification network using the Depthwise Separable convolution and the SE block are designed. Third, a semiautomatic labeling method is proposed for our dataset to improve the efficiency of data labeling. To demonstrate the effectiveness of our method, we first verify the effectiveness of our semiautomatic labeling method through the experiments. And then, we conduct a series of experiments to compare our DLDX with the existing methods. The experimental results demonstrate that our proposed method has fewer Params and Madds and higher detection accuracy than the existing methods.

In future work, we will focus on expanding the types of dangerous liquids and containers and improving our method with dual-view technology to detect dangerous liquids more accurately.

Data Availability

The dataset used to support the findings of this study was supplied by Shenyang DT Inspection Equipment Co., Ltd. in China, under license, and the dataset involving security cannot be shared.

Conflicts of Interest

The authors declare that there are no conflicts of interest regarding the publication of this paper.

Acknowledgments

This work was supported by the National Natural Science Foundation of China (No. 61773106) and Major Scientific and Technological Projects of the Ministry (No. JB2016GD034).

References

[1] X. Zhang, Y. He, T. Chady et al., "CFRP impact damage inspection based on manifold learning using ultrasonic induced thermography," *IEEE Transactions on Industrial Informatics*, vol. 15, no. 5, pp. 2648–2659, 2019.

[2] Y. He, R. Yang, H. Zhang, D. Zhou, and G. Wang, "Volume or inside heating thermography using electromagnetic excitation for advanced composite materials," *International Journal of Thermal Sciences*, vol. 111, pp. 41–49, 2017.

[3] H. Wang, S.-J. Hsieh, X. Zhou, B. Peng, and B. Singh, "Using active thermography to inspect pin-hole defects in anti-reflective coating with k-mean clustering," *NDT & E International*, vol. 76, pp. 66–72, 2015.

[4] Y. He, R. Yang, X. Wu, and S. Huang, "Dynamic scanning electromagnetic infrared thermographic analysis based on blind source separation for industrial metallic damage evaluation," *IEEE Transactions on Industrial Informatics*, vol. 14, no. 12, pp. 5610–5619, 2018.

[5] S. Michel, J. Ruiter, M. Hogervorst, S. Koller, and A. Schwaninger, "Computer-based training increases efficiency in x-ray image interpretation by aviation security screeners," in *Proceedings of the 41st Annual IEEE International Carnahan Conference on Security Technology*, pp. 201–206, Ottawa, ON, Canada, October 2007.

[6] V. Riffo, S. Flores, and D. Mery, "Threat objects detection in x-ray images using an active vision approach," *Journal of Nondestructive Evaluation*, vol. 36, no. 44, 2017.

[7] V. Riffo and D. Mery, "Automated detection of threat objects using adapted implicit shape model," *IEEE Transactions on Systems, Man, and Cybernetics: Systems*, vol. 46, no. 4, pp. 472–482, 2016.

[8] D. Mery, E. Svec, and M. Arias, "Object recognition in x-ray testing using adaptive sparse representations," *Journal of Nondestructive Evaluation*, vol. 35, no. 45, 2016.

[9] T. Franzel, U. Schmidt, and S. Roth, "Object detection in multi-view x-ray images," *Pattern Recognition*, vol. 26, no. 7, pp. 1045–1060, 2012.

[10] Y. Wang, X. Yang, W. Wu, B. Su, and G. Jeon, "An x-ray inspection system for illegal object classification based on computer vision," *International Journal of Security and its Applications*, vol. 10, no. 10, pp. 155–168, 2016.

[11] I. Uroukov and R. Speller, "A preliminary approach to intelligent x-ray imaging for baggage inspection at airports," *Signal Processing Research*, vol. 4, pp. 1–11, 2015.

[12] J. Feng, F. Wang, S. Feng, and Y. Peng, "A multibranch object detection method for traffic scenes," *Computational Intelligence and Neuroscience*, vol. 2019, Article ID 3679203, 16 pages, 2019.

[13] O. Russakovsky, J. Deng, H. Su et al., "Imagenet large scale visual recognition challenge," *International Journal of Computer Vision*, vol. 115, no. 3, pp. 211–252, 2015.

[14] K. He, X. Zhang, S. Ren, and J. Sun, "Deep residual learning for image recognition," in *Proceedings of the 2016 IEEE Conference on Computer Vision and Pattern Recognition*, pp. 770–778, Las Vegas, NV, USA, June 2016.

[15] R. Girshick, J. Donahue, T. Darrell, and J. Malik, "Region-based convolutional networks for accurate object detection and segmentation," *IEEE Transactions on Pattern Analysis and Machine Intelligence*, vol. 38, no. 1, pp. 142–158, 2016.

[16] R. Girshick, "Fast R-CNN," in *Proceedings of the 2015 IEEE International Conference on Computer Vision*, pp. 1440–1448, Santiago, Chile, December 2015.

[17] S. Ren, K. He, R. Girshick, and J. Sun, "Faster R-CNN: towards real-time object detection with region proposal networks," *IEEE Transactions on Pattern Analysis and Machine Intelligence*, vol. 39, no. 6, pp. 1137–1149, 2017.

[18] J. Dai, Y. Li, K. He, and J. Sun, "R-FCN: object detection via region-based fully convolutional networks," in *Proceedings of the 30th International Conference on Neural Information Processing Systems*, pp. 379–387, Red Hook, NY, USA, December 2016.

[19] T. Y. Lin, P. Dollar, R. Girshick, K. He, B. Hariharan, and S. Belongie, "Feature pyramid networks for object detection," in *Proceedings of the 2017 IEEE Conference on Computer Vision and Pattern Recognition*, pp. 936–944, Honolulu, HI, USA, July 2017.

[20] J. Redmon, S. Divvala, R. Girshick, and A. Farhadi, "You only look once: unified, real-time object detection," in *Proceedings of the 2016 IEEE Conference on Computer Vision and Pattern Recognition*, pp. 779–788, Las Vegas, NV, USA, June 2016.

[21] J. Redmon and A. Farhadi, "Yolo9000: better, faster, stronger," in *Proceedings of the 2017 IEEE Conference on Computer Vision and Pattern Recognition*, pp. 6517–6525, Honolulu, HI, USA, July 2017.

[22] J. Redmon and A. Farhadi, "Yolov3: An Incremental Improvement," 2018, https://arxiv.org/abs/1804.02767.

[23] A. Bochkovskiy, C. Y. Wang, and H. Y. M. Liao, "Yolov4: Optimal Speed and Accuracy of Object Detection," 2020, https://arxiv.org/abs/2004.10934.

[24] W. Liu, D. Anguelov, D. Erhan et al., "Ssd: single shot multibox detector," in *Proceedings of the European Conference on Computer Vision*, Amsterdam, The Netherlands, October 2016.

[25] D. Xiao, H. Li, C. Liu, and Q. He, "Large-truck safety warning system based on lightweight SSD model," *Computational Intelligence and Neuroscience*, vol. 2019, Article ID 2180294, 10 pages, 2019.

[26] H. Wan, L. Gao, M. Su, Q. You, H. Qu, and Q. Sun, "A novel neural network model for traffic sign detection and recognition under extreme conditions," *Journal of Sensors*, vol. 2021, Article ID 9984787, 16 pages, 2021.

[27] S. Narejo, B. Pandey, D. E. Vargas, C. Rodriguez, and M. R. Anjum, "Weapon detection using YOLO V3 for smart surveillance system," *Mathematical Problems in Engineering*, vol. 2021, Article ID 9975700, 9 pages, 2021.

[28] D. Mery, E. Svec, M. Arias, V. Riffo, J. M. Saavedra, and S. Banerjee, "Modern computer vision techniques for x-ray testing in baggage inspection," *IEEE Transactions on Systems, Man, and Cybernetics: Systems*, vol. 47, no. 4, pp. 682–692, 2017.

[29] S. Akcay, M. E. Kundegorski, C. G. Willcocks, and T. P. Breckon, "Using deep convolutional neural network architectures for object classification and detection within x-ray baggage security imagery," *IEEE Transactions on Information Forensics and Security*, vol. 13, no. 9, pp. 2203–2215, 2018.

[30] B. Gu, R. Ge, Y. Chen, L. Luo, and G. Coatrieux, "Automatic and robust object detection in x-ray baggage inspection using deep convolutional neural networks," *IEEE Transactions on Industrial Electronics*, vol. 68, no. 10, pp. 10248–10257, 2021.

[31] J. Yang, Z. Zhao, H. Zhang, and Y. Shi, "Data augmentation for x-ray prohibited item images using generative adversarial networks," *IEEE Access*, vol. 7, pp. 28894–28902, 2019.

[32] Y. Zhu, Y. Zhang, H. Zhang, J. Yang, and Z. Zhao, "Data augmentation of x-ray images in baggage inspection based on generative adversarial networks," *IEEE Access*, vol. 8, pp. 86536–86544, 2020.

[33] Y. Zhong, B. Sun, D. Yu et al., "Identification of liquid materials using energy dispersive x-ray scattering," *Proceedia Engineering*, vol. 7, pp. 135–142, 2010.

[34] T. Yangdai and L. Zhang, "Liquid contrabands classification based on energy dispersive x-ray diffraction and hybrid discriminant analysis," *Nuclear Instruments and Methods in*

Physics Research Section A: Accelerators, Spectrometers, Detectors and Associated Equipment, vol. 808, pp. 128–134, 2016.

[35] D. Mery, *Computer Vision for X-Ray Testing*, Springer International Publishing, Manhattan, NY, New York, 2015.

[36] A. G. Howard, M. Zhu, B. Chen et al., "Mobilenets: efficient convolutional neural networks for mobile vision applications," 2017, https://arxiv.org/abs/1704.04861.

[37] M. Sandler, A. Howard, M. Zhu, A. Zhmoginov, and L. C. Chen, "Mobilenetv2: inverted residuals and linear bottlenecks," in *Proceedings of the 2018 IEEE/CVF Conference on Computer Vision and Pattern Recognition*, pp. 4510–4520, Salt Lake, UT, USA, June 2018.

[38] N. Bodla, B. Singh, R. Chellappa, and L. S. Davis, "Soft-NMS-improving object detection with one line of code," in *Proceedings of the 2017 IEEE International Conference on Computer Vision (ICCV)*, pp. 5562–5570, Venice, Italy, October 2017.

[39] A. Howard, M. Sandler, B. Chen et al., "Searching for mobilenetv3," in *Proceedings of the 2019 IEEE/CVF International Conference on Computer Vision (ICCV)*, pp. 1314–1324, Seoul, Republic of Korea, October 2019.

[40] F. N. Iandola, S. Han, M. W. Moskewicz, K. Ashraf, W. J. Dally, and K. Keutzer, "Squeezenet: Alexnet-Level Accuracy with 50x Fewer Parameters and <0.5 mb Model Size," 2016, https://arxiv.org/abs/1602.07360.

[41] J. Hu, L. Shen, S. Albanie, G. Sun, and E. Wu, "Squeeze-and-excitation networks," *IEEE Transactions on Pattern Analysis and Machine Intelligence*, vol. 42, no. 8, pp. 2011–2023, 2020.

[42] V. D. M. Laurens and G. Hinton, "Visualizing data using T-SNE," *Journal of Machine Learning Research*, vol. 9, no. 2605, pp. 2579–2605, 2008.